

The Network Structure of the Corneal Endothelium.

Accepted Manuscript: This article has been accepted for publication and undergone full peer review but has not been through the copyediting, typesetting, pagination, and proofreading process, which may lead to differences between this version and the Version of Record.

Cite as: J. Chem. Phys. (in press) (2022); <https://doi.org/10.1063/5.0134667>

Submitted: 12 November 2022 • Accepted: 29 December 2022 • Accepted Manuscript Online: 02 January 2023

 Bryan Xuan,  Oliver Whitaker and  Mark Wilson



View Online



Export Citation



CrossMark

ARTICLES YOU MAY BE INTERESTED IN

[Quantum dynamics using path integral coarse-graining](#)

The Journal of Chemical Physics **157**, 181102 (2022); <https://doi.org/10.1063/5.0120386>

[Transition state search and geometry relaxation throughout chemical compound space with quantum machine learning](#)

The Journal of Chemical Physics **157**, 221102 (2022); <https://doi.org/10.1063/5.0112856>

[New insights into the early stage nucleation of calcium carbonate gels by reactive molecular dynamics simulations](#)

The Journal of Chemical Physics **157**, 234501 (2022); <https://doi.org/10.1063/5.0127240>



The Journal
of Chemical Physics

Special Topics Open for Submissions

Learn More

The Network Structure of the Corneal Endothelium

Bryan Xuan,¹ Oliver Whitaker,¹ and Mark Wilson^{a1}

¹*Department of Chemistry, Physical and Theoretical Chemistry Laboratory,
University of Oxford, South Parks Road, Oxford OX1 3QZ, UK*

A generic network model is applied to study the structure of the mammalian corneal endothelium. The model has been shown to reproduce the network properties of a wide range of systems, from low-dimensional inorganic glasses to colloidal nanoparticles deposited on a surface. Available extensive experimental microscopy results are analysed and combined to highlight the behaviour of two key metrics, the fraction of hexagonal rings (p_6) and the coefficient of variation of the area (CV). Their behaviour is analysed as a function of patient age, the onset of diabetes and contact lens wearing status. Wearing contact lenses for ~ 10 years is shown to change the endothelium structure by the equivalent of ~ 30 years contact lens-free. Model network configurations are obtained using a Monte Carlo bond-switching algorithm with the resulting topologies controlled by two potential model parameters (the bond and angular force constants) and the Monte Carlo temperature. The effect of systematically varying these parameters is investigated. In addition, the effect of constraining the ring size distribution is investigated. The networks generated with relatively weak bond force constants are shown to correlate best with the experimental information. The importance of extracting the full ring size distribution (rather than simply the fraction of hexagons) is discussed.

^a mark.wilson@chem.ox.ac.uk

I. INTRODUCTION

The cornea is a transparent avascular membrane comprised mainly of collagen molecules which form the anterior section of the eye^{1,2}. The membrane forms a crucial barrier to both infection and structural damage and is constructed from five distinct layers. In this paper we are concerned with one of these layers, the corneal endothelium, which can be readily imaged and which adopts a honeycomb-like structure. Such structures are common across a range of systems, from the atomic level of ultra-thin materials³⁻⁵, through colloids^{6,7}, foams^{8,9}, epithelial cells^{10,11} and all the way to geological rock formations¹². The maturing of network science as a field has led to new ways of thinking about, and quantifying, complex networks¹³ driven largely by interest in abstract networks such as the internet or social media^{14,15}. The corneal endothelium is potentially another example of such a network. At a fundamental level the endothelium structures (as well as those systems listed above) appear to map onto a percolating network of rings or, equivalently, to an array of connected nodes and hence they are governed by the same fundamental laws. For the percolating ring network description, for example, the structure can be characterised (at one level) by determining the number of rings of different size, where the ring size corresponds to the number of edges in that ring. In addition, the areas of the rings can be measured and their deviation from ideal regular polygons can be quantified, for example, by determining the coefficient of variation of the area. Experimental evidence suggests that the structure of the corneal endothelium is affected not only by aging¹⁶⁻²⁶, but by other factors such as the onset of diabetes²⁷⁻³⁰, smoking status³¹ or the prolonged wearing of contact lenses³²⁻³⁵. The most common network properties which are tracked experimentally are the cell density, the distribution of ring sizes (cellular polymorphism) and the distribution of the areas of those rings, in particular distortions away from their ideal (symmetric) shapes (cellular pleomorphism). These systems may show additional structural complexity. The rings in a given ring size distribution may be arranged in an effectively infinite number of ways. For chemical systems it is intuitive that some configurations would be expected to be energetically favourable. For example, at the nearest-neighbour length-scale, it is reasonable to assume that large rings will tend to be located next to small rings. It is also likely that structural ordering may persist beyond the nearest-neighbour length-scale.

In this paper we aim to make connections between the experimental information available for the corneal endothelium structure and network theory to demonstrate how better to quantify their structure, thus allowing connections to be made to a wide range of related systems. The connections made may help rationalise some experimental observations, for example, quantifying how corneal damage from non-aging mechanisms correlates with that resulting from aging alone. In addition, the construction of model networks allows insight into any ordering of the rings which may be quantified, again by reference to network theory using the assortativity³⁶⁻³⁸.

The outline of this paper is as follows. In section II the background to the required network theory is summarised. In section III the methods used will be discussed. Section IV will contain the results, dividing into the analysis of the experimental information, the construction and analysis of model networks and finally a discussion of the links between the two. Finally, conclusions will be drawn.

II. BACKGROUND

The network topology is described by Euler's formula, $N + V - E = \chi$, where N , V and E are the number of rings, vertices and edges, and χ is the so-called Euler characteristic, which depends on the global topology of the system. Consider a network constructed from nodes with a range of coordination numbers, c , with the fraction of each given by x_c . As a result, the mean coordination number is $\langle c \rangle = \sum_c c x_c$. The number of edges is then $E = \frac{V}{2} \langle c \rangle$ and the mean ring size is $\langle k \rangle = \frac{V}{N} \langle c \rangle$. Euler's formula may then be rewritten as

$$\langle k \rangle = \frac{2\langle c \rangle (1 - \frac{\chi}{N})}{\langle c \rangle}. \quad (1)$$

As a result, for $\langle c \rangle = 3$ (nodes of degree three) and $\chi = 0$ (corresponding to an infinite plane), the mean ring size, $\langle k \rangle = 6$.

The next level of available information is given by the ring size distribution, p_k (the distribution of different ring sizes in a given network). Lemaître *et al.* demonstrated how many three-coordinate networks can be described by a maximum entropy distribution³⁹. In summary, the entropy of the probability distribution is $S = -\sum_k p_k \log p_k$, and the system is subject to three constraints; $\sum_k p_k = 1$, $\sum_k k p_k = \langle k \rangle$, and $\sum_k \frac{p_k}{k} = \text{constant}$. The first two constraints correspond to the distribution being normalised and the requirement of a fixed mean ring size. The third constraint is a little more mysterious and was originally justified through the ring areas, although it can be fully justified by considering the ring adjacencies⁴⁰. As a result the distribution can be summarised through the variance, $\mu_2 = \langle k^2 \rangle - \langle k \rangle^2$, and the plot of μ_2 vs. p_6 is known as Lemaître's law.

For a more constrained system of three types of ring, $k = \{5, 6, 7\}$ only, the constraint that $\langle k \rangle = 6$ requires that $p_5 = p_7$ and so,

$$\begin{aligned}\mu_2 &= \sum_{k=5}^7 k^2 p_k - \left\{ \sum_{k=5}^7 k p_k \right\}^2 = \sum_{k=5}^7 k^2 p_k - 36, \\ &= 5^2 p_5 + 6^2 p_6 + 7^2 p_7 - 36 = 74 p_5 + 36 p_6 - 36.\end{aligned}\quad (2)$$

The distribution given by p_k is normalised such that $p_5 + p_6 + p_7 = 1$, and so $2p_5 = 1 - p_6$. As a result,

$$\mu_2 = 37(1 - p_6) + 36p_6 - 36 = 1 - p_6. \quad (3)$$

In this case, therefore, the Lemaître curve is simply linear in p_6 and so a single measurement of p_6 fully defines the ring size distribution *including* the precise number of 5- and 7-membered rings.

For a less constrained distribution, in which both smaller and larger rings are permitted, μ_2 may become larger and depend on p_6 in a non-linear fashion. Again, however, if the ring sizes follow a maximum entropy distribution then measuring p_6 alone still fully defines the fractions of the remaining ring sizes, $p_{k'} (k' \neq 6)$. Configurations which do not sit on the Lemaître curve may do so either because of a finite system size effect or because the ring size distribution does not reflect the maximum entropy solution (*i.e.* enthalpic effects are significant). It is worth noting that not all ring size distributions fit on this curve. The most obvious examples are (ordered) crystalline networks, such as the complete tiling of space by $\{4-, 8-\}$ membered or $\{3-, 12-\}$ membered rings respectively (see ref.⁴¹ and references therein). Recent work has shown how so-called procristalline structures, in which sites on an ordered lattice are linked by a disordered array of bonds, may also ‘violate’ Lemaître’s law⁴².

The ring size distribution does, however, give an incomplete picture of the overall network structure. The rings in a given distribution may be arranged in an arbitrarily (infinite) number of ways. It is, however, physically reasonable to assume that some configurations will be energetically favoured over others. For example, large rings should tend to be nearest-neighbours to small rings. For systems with chemical bonds the background to this behaviour is clear as the relatively obtuse bond angles associated with larger rings needs to be “offset” by the more acute angles associated with smaller rings in order to avoid significantly strained bonds and/or angles. The magnitude of any such nearest-neighbour ordering can be quantified. Historically, the mean ring size around a given ring was determined, leading to the Aboav-Weaire law^{43,44}. In that case the degree of association is characterised by a single parameter (usually given the symbol α). However, the limits of this parameter are unclear and obtaining it requires a linear fit (which may not be appropriate) and is heavily dependent upon (potentially small numbers) of small and/or large rings⁴⁵. Furthermore, the parameter is not zero for a totally disordered network. An alternative metric is the assortativity, r , commonly employed in network theory and which has clear limits (of ± 1), a value of $r = -1$ corresponding, for example, to a fully disassortative network³⁶. In the present work we shall refer exclusively to the assortativity.

III. METHODS

The chosen method for generating randomised ring size distributions is via a bond-switching algorithm, a Monte Carlo stochastic sampling approach originally developed by Wooten, Winer and Weaire to generate models for silica glass in three dimensions⁴⁶. Analogous approaches have been employed for 3-coordinate, and in one instance 4-coordinate, planar atomic systems^{47,48}. In the present work the starting configuration is an ideal hexagonal net (equivalent to a graphene sheet or a honeycomb). To amorphise the network links between neighbouring nodes are switched and the change in potential energy of the system is calculated. The potential energy is a relatively simple function of the atom positions. Incorporating switches which reduce the network potential energy with greater probability biases the search towards low energy networks. The original hexagonal lattice is thermalised using a large number of random bond switches to generate a random network with high energy which has no “memory” of the original ordered lattice. The system is then annealed at finite temperature, T , by accepting moves according to the Metropolis criterion⁴⁹:

$$P = \min \left[1, e^{-\Delta U / k_B T} \right]. \quad (4)$$

ΔU is the change in energy resulting from the proposed move. The net effect will be to accept more moves which reduce the system energy and hence generate a physically-acceptable network structure.

The bond-switching move (known as a T1 switch⁵⁰ or, more recently, as a Stone-Wales defect⁵¹) augments the ring size of two rings and decrements two others, preserving the mean ring size.

The system energy is determined using a specified potential model, here a simplified two-dimensional version of the Keating potential⁵² augmented with a restricted bending (ReB) potential⁵³ of the form:

$$U = \sum_{i,j \in \text{bonds}} \frac{k_r (r_{ij} - r_0)^2}{2} + \sum_{i,j,k \in \text{angles}} \frac{k_\theta (\cos \theta_{ijk} - \cos \theta_0)^2}{f(\theta_{ijk})}, \quad (5)$$

where r_0 is the equilibrium separation between neighbouring nodes and θ_0 the equilibrium angle between pairs of neighbouring nodes, and k_r and k_θ are the respective bond and angle force constants, which control the relative magnitudes of the bond length and angular components of the total potential energy. The equilibrium bond length was set equal for all interaction types and the equilibrium angles were set to $2\pi/3$ radians, appropriate for the three-coordinate nodes. The function $f(\theta_{ijk}) = 2\sin^2 \theta_{ijk}$ for the ReB potential (setting $f(\theta_{ijk}) = 1$ recovers the simplified Keating potential). The ReB angle potential maintains ring convexity. The addition of the sine term in the denominator causes the potential to diverge as bond angles approach linearity, and so prevents the bond pairs from “inverting”. The rationale for choosing a relatively simple potential of this form is that a key aim is to obtain results for generic systems, which captures the essential physics, whilst remaining computationally tractable to allow a high-throughput approach. The simplicity of the chosen potential model means that the network topology and the shape of the contributing rings are controlled by just three parameters, the bond length and angle force constants (k_r and k_θ respectively) and the system temperature, T . In fact, the system is further constrained in the sense that the energy scale imposed by the choice of force constants is linked to the available thermal energy. Put simply, increasing the force constants can be “offset” by increasing the temperature. As a result, the key network properties can be systematically varied by varying, say, k_r , the ratio k_θ/k_r and T . The expectation would be that varying the ratio k_θ/k_r could help transform the system from one which is more like atomic material (*i.e.* length dominated) to a foam (angle dominated). For example, Wooten *et al.* suggested values for k_θ/k_r of 0.2⁵⁴ and 0.285⁴⁶ respectively to study amorphous Si and Ge whilst Martin investigated the properties of a range of ZnS structure semiconductors using $k_\theta/k_r = 0.294 - 0.079$ ⁵⁵, and Kumar *et al.* modelled amorphous graphene with $k_\theta/k_r = 0.2$ ⁵⁶. k_r and k_θ are systematically varied with $k_r = \{0.010, 0.2, 0.4, 0.6, 0.8, 1.0\}$ and $k_\theta = \{0.1, 0.15, 0.2, 0.25, 0.3\}$. As an additional control the range of rings “allowed” to form is varied with three systems considered. In the first, the ring sizes are unconstrained, whilst in the other two the ring sizes are constrained to be between 5- and 7-membered and 4- and 8-membered (termed {567} and {45678} respectively).

IV. RESULTS

A key motivation in the present work is to attempt to link state of the art models and techniques to existing experimental results. As a result, section A will present a survey of available experimental data, focussing on the key extracted topological parameters and highlighting any possible trends. Section B will focus on the simulation model results and how these may relate back to the experimental data.

A. Interpretation of the Experimental data

The most common experimental data presented are in the form of the fraction of hexagons, p_6 , less commonly given with a more complete analysis of the ring size distribution, the ring areas, and the coefficient of variation (CV) of the area, $CV = \sigma_A/\bar{A}$, where σ_A and \bar{A} are the standard deviation and mean area respectively.

1. Trends in p_6

Figure 1(a) shows a schematic to highlight the range of p_6 values obtained from experiment. The data are subdivided into those obtained as a function of patient age^{16–26}, contact lens usage^{32–35}, onset of diabetes^{27–30}, and “other” (here, covering smoking behaviour, non-human species (here, dogs, rabbits and mice) and the behaviour of transplanted tissue^{22,31,57–61}). A large spread of p_6 values are obtained, ranging from $p_6 \sim 0.36 - 0.88$. The most significant factor affecting p_6 appears to be aging ($p_6 \sim 0.39 - 0.88$). The wearing of contact lenses and diabetes show a similar, but smaller, range ($p_6 \sim 0.54 - 0.71$ and $p_6 \sim 0.52 - 0.68$ respectively). The points labelled “other” cover the range $p_6 \sim 0.36 - 0.83$.

As discussed in the introduction, a range of different systems show this type of ring structure and display different ranges of values for p_6 ⁴⁰. For example, colloidal nanoparticles distributed on a surface show $p_6 \sim 0.35 - 0.69$ depending on the packing fraction, whilst thin layers of silica and graphene show $p_6 \sim 0.42 - 0.46$ and $p_6 \sim 0.55 - 0.95$

respectively. For reference, the Poisson-Voronoi limit, which corresponds to a random distribution of points on a surface (or, equivalently, the limit as the packing fraction of the colloids on a surface tends to zero) corresponds to $p_6 \sim 0.295$. Even more extreme distributions can be obtained by considering, for example, geographical entities such as county boundaries of political constituencies, which show relatively low values of p_6 ($p_6 \sim 0.21 - 0.28$)⁴⁰. Figure 1(b) shows the spread of experimentally-determined p_6 values on a Lemaître curve (a plot of the standard deviation of the ring size distribution, μ_2 , against p_6) assuming the presence of 5-, 6- and 7-membered rings only (which, recall from section II, imposes a linear relationship of $\mu_2 = 1 - p_6$). The figure also shows the ideal Lemaître curve obtained from the maximum entropy solution for an unconstrained ring size distribution. The ideal curve is linear for $p_6 \gtrsim 0.6$ for which the networks are dominated by 5-, 6- and 7-membered rings only. The curve deviates from linearity for $p_6 \lesssim 0.6$ as the networks contain a broader range of ring sizes.

Experimental data obtained as a function of patient age are shown in figure 2(a). The data are subdivided by the nation of origin of the patient with the published standard deviations shown as error bars^{16–22,25,62,63}. In the majority of cases the fraction of six-membered rings decreases as a function of time (and this is the over-arching trend in all cases). The aging of the network appears correlated with the degradation away from an ideal hexagonal network. The figure also highlights the mean average curve calculated as a simple unweighted average of all the data shown. The mean shows a steady decline in p_6 to $t \sim 35$ years, followed by a levelling off. One possibility is that this corresponds to the value of p_6 below which rings of size other than 5-, 6- and 7-membered are required (which would correspond to the value at which the Lemaître curve shown in figure 1(b) deviates from the linear constrained maximum entropy solution).

Figure 2(b) shows additional data to that shown in panel (a) obtained for mice over their lifespan²². In order to allow comparison with the data obtained for humans the abscissa are normalised by the approximate lifespans (taken as $t_{\text{lifespan}} \sim 80$ years for humans and ~ 2.5 years for mice respectively). The data obtained from mice show a reduction in p_6 at long times ($t/t_{\text{lifespan}} \gtrsim 0.1$) but show a rise at short time corresponding to the continued eye development in mice *post partum*. The implication is that the networks degrade relatively little over the lifespan of the animal and the rate of change is related to the animal lifespan (and hence metabolic rate).

Figure 2(c) shows the result of an attempt to generate a “universal” curve for the change in p_6 with age. Each experimental data are normalised such that $p_6 = 1$ at $t \rightarrow 0$, corresponding to starting from an ideal hexagonal net. p_6 shows a near linear decrease to a reduced age of $t_{\text{red}} \sim 0.4$ (corresponding to $t \sim 32$ years in humans) with gradient $dp_6/dt \sim -0.0046\text{year}^{-1}$. Beyond this age some groups show a further (slower) decrease in p_6 whilst others appear to have reached a limiting value.

In addition to the passage of time, external factors such as contact lens wearing, smoking status or the onset of diabetes may affect cornea endothelium structure. Figure 3(a), for example, shows the mean average temporal behaviour of p_6 on aging (from figure 2(a)) compared to two studies in which the effect of contact lens wearing is investigated^{32,33}. In both cases the fraction of hexagonal cells is determined as a function of the period for which the lenses have been worn. Lee *et al.*³³ studied the effect of wearing soft contact lenses in the age group $t \sim 25 - 31$ years with between zero and $\Delta t \sim 14$ years of continual wear, whilst Chang *et al.*³² considered a group in the age range $t \sim 23.6 - 27.0$ years old with between zero and 8.3 years wear. In both cases the fraction of hexagons appears to decrease significantly over a ten year time-scale. For context, figure 3(b) shows the same data displaced along the time axis by the mean age of the participants and compared to the mean average behaviour of the aging data from figure 2(a). It is clear that the fraction of six-membered rings falls more rapidly for the contact lens wearers when compared with the aging process alone. To quantify the effect a simple linear fit to the whole data sets produces rates of change of $dp_6/dt = -0.0113\text{year}^{-1}$ and $dp_6/dt = -0.0152\text{year}^{-1}$ for the data of Lee *et al.*³³ and Chang *et al.*³² respectively, compared with $dp_6/dt = -0.0046\text{year}^{-1}$ for the aging process (see above). The endothelium network also appears more disordered as a result of contact lens wearing in older patients. Figure 3(b) shows the data of Nieuwendaal *et al.*³⁴ who report a change from $p_6 \sim 0.68 \pm 0.06$ to $p_6 \sim 0.56 \pm 0.07$ for humans in the age range ~ 41 -42 years. Figure 3 also shows data from Bourne *et al.*^{57,58} who studied changes in the endothelium morphology in transplanted corneas up to ~ 20 years post-surgery. The rate of change is $dp_6/dt = -0.0081\text{year}^{-1}$, comparable to the effect of contact lens wearing and significantly higher than that attributable to aging alone. Overall, therefore, wearing contact lenses for ten years appears to lead to an equivalent change in the corneal endothelium structure of $\simeq 30$ years by aging alone. Similarly, the transplanted corneas age the equivalent of $\simeq 20$ years over the ten year time-scale.

The effect of the onset of diabetes appears more subtle. Taşlı *et al.*³⁰ find a change from $p_6 = 0.7849 \pm 0.0656$ to $p_6 = 0.6694 \pm 0.0717$ for patients with and without diabetes. In this study the mean age of the control and diabetic patients was $t = 59.6$ and $t = 61.4$ years respectively. Chowdhury *et al.* see a smaller change, from $p_6 = 0.5694 \pm 0.0700$ to $p_6 = 0.5534 \pm 0.0582$ for the control and diabetic patients in a younger age group of $t = 53.7 \pm 7.0$ and $t = 53.3 \pm 6.0$ years respectively²⁷. Kim and Kim²⁸ studied the effect of diabetes grouped by patient age (from $t \sim 40$ to $t > 80$ years), showing a small further decrease in p_6 in older diabetic patients. For example, patients in the $t = 40 - 49$ years group showed $p_6 = 0.554 \pm 0.020$ and $p_6 = 0.555 \pm 0.020$ for the control and diabetic groups respectively, whilst patients of age $t > 80$ years showed $p_6 = 0.530 \pm 0.020$ and $p_6 = 0.508 \pm 0.020$. It appears, therefore, that the effect

of the onset of diabetes becomes more significant with patient age.

Smoking status appears to lead to a similar (small) change. Golabchi *et al.*³¹ report a change from $p_6 = 0.5042 \pm 0.0861$ to $p_6 = 0.4829 \pm 0.0848$ for the control and smoking groups (mean ages, $t \sim 46.39$ years and $t \sim 48.61$ years respectively). Again, in terms of aging time-scales, this implies the corneal endothelium in the eye of a smoker will age the equivalent of $\simeq 17$ years over a 10 year time-frame.

2. The effect of using p_6 only

Figure 1 shows a range of p_6 values obtained from experimental investigations. In panel (b) the data are shown in the form of a Lemaître curve (*i.e.* as the variance, μ_2 , *vs.* p_6 which, as described above, highlights the deviation of the ideal (maximum entropy) curve from linearity for $p_6 \lesssim 0.6$ and which corresponds to networks containing both 4-membered rings and rings larger than 7-membered). In panel (a) the data are sub-divided by the focus of the experiment (aging, the wearing of contact lenses and the onset of diabetes) whilst panel (b) shows the data sub-divided by patient nationality and includes data obtained for diabetic dogs⁶⁰, injured rabbits⁶¹ and aging mice²². Figure 4(a) shows a Lemaître curve highlighting experimental data for which a more complete distribution of ring sizes has been published^{18,26,60,61,64–66}. The relatively small system sizes lead to relatively large error bars making definitive conclusions difficult to draw. For example, the finite system size need not lead to a mean ring size of six. It is clear, however, that the vast majority of the observations for $p_6 \gtrsim 0.6$ sit on the linear region of the Lemaître curve. It is reasonable to expect that the error bars associated with the small system sizes will be larger for the more diverse distributions of ring sizes (smaller p_6). As noted above (section II) it is entirely possible for ring size distributions to not sit on the maximum entropy solution if non-entropic (entropic) effects are significant. It remains to be seen if this is the case here.

3. Cell Areas

Figure 5(a) shows the variation of the cell area coefficient of variation, CV , with human patient age (data from refs.^{16–23,25,26,67,68}). CV rises gradually, and near-linearly, with age with mean gradient $d(CV)/dt \sim 0.001\text{year}^{-1}$. The increase in CV is potentially indicative of both the broadening of the ring size distribution (fall in p_6) and a reduction in ring regularity. Figure 5(b) shows the same data normalised for lifespan and including additional data for cats⁶⁸ and mice²². The smaller mammals show a similar *change* in CV over their respective lifespans. The magnitude of the CV appears to reduce with mammal lifespan. Figure 4(b) shows the experimental CV against the fraction of hexagons, p_6 . The figure also shows the analytic maximum entropy solutions (see appendix VII) determined for the constrained 5-, 6- and 7-membered ring system and for the unconstrained ring size distribution and assuming that the polygons adopt their ideal areas. The experimental data shows a CV whose dependence on p_6 effectively mirrors the analytic ideal solution but is systematically larger, perhaps reflecting the distortions of the contributing polyhedra from their ideal (regular) shapes.⁶⁹

B. Model Behaviour

1. p_6 and CV

As outlined in section III, the networks obtained from the bond-switching algorithm are controlled by three parameters; the bond length and angle force constants (k_r and k_θ respectively) and the Monte Carlo temperature, T . Varying these parameters allows us to control the level of disorder and topologies of the generated networks. Figure 6 shows the Lemaître curve obtained over the full range of $\{k_r, k_\theta, T\}$ investigated here. As the Monte Carlo temperature increases the distribution of ring sizes becomes broader corresponding to higher μ_2 (lower p_6). At low T the network corresponds to a near-ideal hexagonal net ($p_6 = 1$) with a corresponding vanishingly small CV . As T increases the fraction of hexagons falls (corresponding to the formation of networks dominated by hexagons with isolated 5- and 7-membered ring defects). The figure also shows the analytic (maximum entropy) solutions for the constrained $\{567\}$ and $\{45678\}$ rings system and the unconstrained ring size distribution. As discussed in section II, the $\{567\}$ constrained system shows a linear dependence with $\mu_2 = 1 - p_6$. The $\{45678\}$ system shows a non-linear dependence but sits below the ideal maximum entropy solution at very low p_6 ($p_6 \lesssim 0.45$) as even larger rings ($k > 8$) become entropically favoured.

Figure 7(a) shows the values for the CV of area obtained from the simulation models for all values of $\{k_r, k_\theta, T\}$ investigated. The figure show the ideal values calculated from both equations 7 and 11 (see Appendix). As $p_6 \rightarrow 1$,

$CV \rightarrow 0$ as the network is comprised exclusively from ideal hexagons. As p_6 falls CV increases simply reflecting the dispersion of polygon areas imposed by the presence of 5- and 7-membered rings. For the constrained system, $CV \rightarrow \frac{|A_5 - A_7|}{A_5 + A_7} \sim 0.36$ as $p_6 \rightarrow 0$ (*i.e.* for a system composed of 5- and 7-membered rings only). For the unconstrained network CV continues to rise as p_6 is reduced, reflecting the presence of an increasing diversity of different sized rings. The obtained model values mirror the ideal curve (see Appendix) with higher values, reflecting the distortions of the polygons from their ideal areas. As for figure 6, data are shown for the three differently constrained systems. As the level of constraint is reduced (corresponding to moving between $\{567\} \rightarrow \{45678\} \rightarrow$ unconstrained networks) CV is able to increase more rapidly as p_6 decreases, corresponding to the formation of both smaller and larger rings. The figure also shows the ideal CV curves for both the $\{567\}$ and unconstrained networks (see Appendix). Figure 7(b) shows the values for the CV for five values of k_r (over all values of k_θ) ranging from $k_r = 0.01 - 1.0$. As k_r is reduced (corresponding to making the bonds less strong) CV is observed to deviate from the ideal curves as the greater distribution of bond lengths facilitates more distorted polygons. Figure 7(c) shows the values for the CV for three values of k_θ (over all values of k_r) with $k_\theta = 0.1 - 0.3$. As k_θ is reduced CV increases corresponding to the weaker angular constraint facilitating greater polygon distortions.

To better see these differences we can define a difference function as $\Delta CV = CV - CV_{id}$, where CV is obtained from the model or directly from experiment, and CV_{id} is the ideal value assuming regular polygon areas. Figure 7(d) shows ΔCV *vs.* p_6 for the model data, coloured by k_r , corresponding to the ‘raw’ CV data shown in figure 7(b). As k_r is reduced (corresponding to a weakening of the node-node “bond strength”) ΔCV increases reflecting the greater polygon distortion. As $p_6 \rightarrow 1$ then $\Delta CV \rightarrow 0$, corresponding to an ideal hexagonal net. At exceptionally low values of p_6 ($p_6 \lesssim 0.25$) ΔCV can become negative, reflecting the presence of larger rings which can be more easily distorted. Figure 7(d) also highlights the values of ΔCV obtained from the experimental data (and corresponding to the data shown in figure 4(b)). The observed experimental values appear to correlate most strongly with the simulated values obtained using weaker bond force constants.

2. Nearest-neighbour structure

Figure 8 shows a set of molecular graphics “snapshots” corresponding to different values of k_r and k_θ . The effect of changing the relative strengths of the bond and angular force constants is clear “by eye”. The combination of the strongest bond force constant and weakest angular force constant (top left panel, corresponding to $k_\theta/k_r = 0.1$) generates a network with a wider distribution of bond angles. The combination of relatively strong bond and angular force constants (bottom right panel) generates a much more regular looking network. Whilst the difference in structure is clearly visible in terms of, for example, the deformation of the individual polygons, any difference in nearest-neighbour structure is more difficult to effectively quantify. As noted in section III the assortativity, r , represents a useful metric for characterising any nearest-neighbour structural ordering. A further simple measure is to consider the pairwise structure of the ring system, that is, count the number of rings of size k which surround a ring of size k' . These ring adjacencies then build up to form the overall assortativity. However, a simple visualisation procedure is flawed for considering the assortativities as they are complex averages over all ring size pairs.

Figure 9 shows the change in assortativity with p_6 as a function of (a) k_θ at five fixed values of k_r and, (b) k_r at three fixed values of k_θ . In all cases the choice of force constants has a significant effect on the resulting assortativity. The range of assortativities obtained is relatively large, spanning $-0.28 \lesssim r \lesssim -0.10$. For comparison, typical values for related systems include: colloids - $-0.25 \lesssim r \lesssim -0.18$, silica - $-0.34 \lesssim r \lesssim -0.32$, graphene - $-0.27 \lesssim r \lesssim -0.22$. At first glance, therefore, it appears that the simulated networks generated here correspond most clearly, as might be expected, to the colloidal networks. At fixed k_θ an increase in k_r makes the assortativity more negative (corresponding to a stronger preference for small-large neighbouring rings), whilst at fixed k_r an increase in k_θ appears to have the opposite effect.

The precise structural origins of changes in assortativity can be difficult to isolate as all pairs of rings contribute. One potential method is to count the numbers of given nearest-neighbour pairs and compare them to the expected values assuming a random distribution of rings. For example, figure 9(c) shows the change in the number of nearest-neighbour ring size pairs, $\{kk'\}$, as a function of k_r at fixed k_θ . Increasing k_r at fixed k_θ increases the number of nearest-neighbour $\{57\}$ pairs with a concomitant reduction in the number of $\{77\}$ pairs, both leading to a more negative assortativity. The effect of changing k_θ at fixed k_r is more subtle.

V. DISCUSSION

The application of a generic model to a key biological problem facilitates an understanding of the network structure in the broader context of related systems. One of the key reasons for wishing to develop a network model is to help

interpret the abundance of available experimental data. By systematically varying the model parameters networks which resemble those observed experimentally have been obtained. Models which employ relatively weak bond force constants (low k_r) show the most favourable comparison with experimental data, in particular in terms of the polygon areas (as measured by the respective coefficient of variation). This places the corneal endothelium networks in the same “class” as those formed by colloidal nanoparticles deposited on surfaces or by foams on surfaces, as distinct to structures formed by low-dimensional glasses or ultrathin materials.

The most commonly experimentally-measured property is the fraction of hexagons, p_6 . However, it is clear that is important to determine the full ring size distribution. For a maximum entropy distribution the determination of p_6 alone *does* automatically generate the ring size distribution, but non-entropic effects can alter the distribution in a non-trivial fashion. For example, the analysis of the decay of p_6 with patient aging hints at p_6 reaching a potential plateau at $p_6 \sim 0.6$. This value corresponds to the region of the Lemaître curve where the maximum entropy solution deviates significantly from linearity. Supporting values of $p_6 \lesssim 0.6$ requires the stabilisation of relatively small (4-membered) and relatively large ($k > 7$) rings. The implication of a plateau in p_6 with patient age is that the formation of such small and large rings is affected by non-entropic effects.

Finally, connections with more general network theory potentially allows additional structural information to be obtained. The assortativity, for example, quantifies the nearest-neighbour ring structure and highlights a preference for small rings to be neighbours to large rings and *vice versa*. Experimental observation of large enough samples should allow this key metric to be extracted including, critically, its behaviour with patient aging.

Having noted potential improvements in experimental measurements, coupled with symbiotic model development, it is important to note that the models themselves can be significantly improved. Real corneal endothelia, for example, show polygon areas which change with patient aging owing to cell recombination effects. Such “moves” can be incorporated as additional potential Monte Carlo rearrangements and this will form the basis of future work.

VI. CONCLUSIONS

In this paper a relatively simple bond-switching Monte Carlo method has been applied to generate a wide range network structures. These networks have been compared to data extracted from the study of the mammalian corneal endothelium. The ability to systematically vary the model parameters allows the structural characteristics of these systems to be assessed alongside analogous network-formers. Indeed, network theory has been most commonly applied to problems more traditionally associated with physics, materials science and chemistry (or at the respective interfaces). Models employing relatively weak bond force constants have been found to be most appropriate, mapping these systems more clearly onto two-dimensional layers of colloidal nanoparticles. In addition, the work highlights how more useful information could be extracted from experimental investigations, for example, extracting details of the nearest-neighbour structure.

ACKNOWLEDGEMENTS

We are grateful for support from the EPSRC Centre for Doctoral Training in Theory and Modelling in Chemical Sciences (TMCS), under grant EP/L015722/1. MW is grateful to Dr. Martin Galpin for helpful discussions. This paper conforms to the RCUK data management requirements.

VII. APPENDIX: COEFFICIENT OF VARIATION OF THE AREA

Consider an ideal k -polygon with sides of length $r_0 = 1$. The ideal area is

$$A_k^o = \frac{k}{4\tan(\pi/k)}. \quad (6)$$

We want to determine the coefficient of variation (CV) of the area, $CV = \frac{\sigma_A}{\bar{A}}$, as the ring size distribution changes (*i.e.* purely as the effect of having a mixture of different areas for the different k -rings). The n^{th} moment of the area is given by $\langle A^n \rangle = \sum_k A^n p_k$ and so,

$$CV = \frac{\left[\sum_i p_i A_i^2 - (\sum_i p_i A_i)^2 \right]^{1/2}}{\sum_i p_i A_i}. \quad (7)$$

Let us assume only 5- to 7-membered rings for simplicity. So,

$$\bar{A} = p_5 A_5 + p_6 A_6 + p_7 A_7. \quad (8)$$

For this system we have the usual constraints of $p_5 = p_7$ (as $\bar{n} = 6$) and $p_5 = \frac{1-p_6}{2}$ as $\sum_i p_i = 1$. As a result,

$$\begin{aligned} \bar{A} &= \frac{(1-p_6)}{2}(A_5 + A_7) + p_6 A_6 \\ &= \frac{(A_5 + A_7)}{2} + p_6 \left[A_6 - \frac{1}{2}(A_5 + A_7) \right]. \end{aligned} \quad (9)$$

$$\bar{A}^2 = \frac{(A_5^2 + A_7^2)}{2} + p_6 \left[A_6^2 - \frac{1}{2}(A_5^2 + A_7^2) \right], \quad (10)$$

and so, CV can be written as

$$CV = \frac{\left\{ \frac{(A_5^2 + A_7^2)}{2} + p_6 \left[A_6^2 - \frac{1}{2}(A_5^2 + A_7^2) \right] - \left(\frac{(A_5 + A_7)}{2} + p_6 \left[A_6 - \frac{1}{2}(A_5 + A_7) \right] \right)^2 \right\}^{1/2}}{p_5 A_5 + p_6 A_6 + p_7 A_7}. \quad (11)$$

Figure 7 shows CV vs. p_6 calculated from both equations 7 and 11. As $p_6 \rightarrow 1$, $CV \rightarrow 0$ as the network is comprised exclusively from ideal hexagons. As p_6 falls CV increases simply reflecting the dispersion of polygon areas imposed by the presence of 5- and 7-membered rings. For the constrained system, $CV \rightarrow \frac{|A_5 - A_7|}{A_5 + A_7} \sim 0.36$ as $p_6 \rightarrow 0$ (*i.e.* for a system composed of 5- and 7-membered rings only). For the unconstrained network CV continues to rise as p_6 is reduced, reflecting the presence of an increasing diversity of different sized rings.

Equations 7 and 11 require values for the ideal ring areas. At the simplest level the ideal values from equation 6 can be applied. However, other than for the ideal hexagonal net, the ring areas will not actually take these values. An alternative, for example, is to use values of A_5 and A_7 obtained from a single bond switch. This has the advantage that the area is conserved (as a single switch converts four hexagons into two heptagons and two pentagons and so $4A_6 = 2A_5 + 2A_7$).⁷⁰ The ideal curve using these values for A_5 and A_7 are shown in figure 7(a) for the constrained system and, significantly, shows little difference to the curve obtained using the ideal areas. In conclusion, the detailed choice of polygon areas has little effect on the predicted CV.

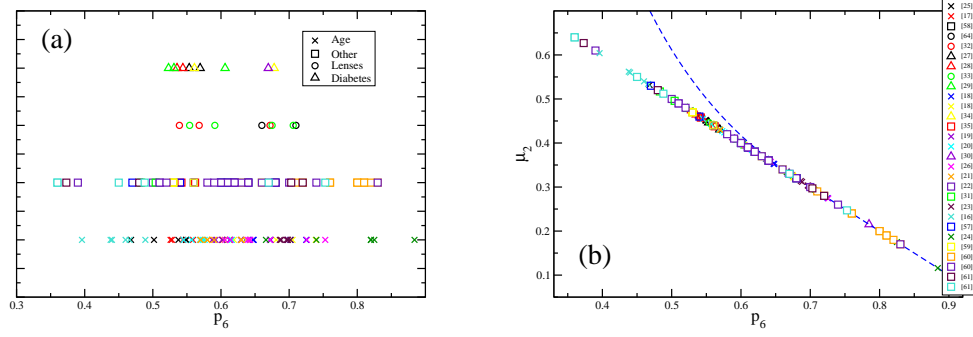


FIG. 1. Alternative views of the experimental observations of the fraction of hexagons, p_6 , in the corneal endothelium. In panel (a) the data are subdivided in term of patient age (\times), contact lens wearing (\circ), diabetic status (Δ) and "other" (\square) - see text. The four divisions are offset along the ordinate axis for clarity. In panel (b) The same data are shown on a Lemaître curve showing the variance, μ_2 , assuming a constrained system containing 5-, 6- and 7-membered rings only (giving $\mu_2 = 1 - p_6$). The dashed line shows the maximum entropy solution assuming an unconstrained ring size distribution. The respective references are shown in the legend and apply to both panels.

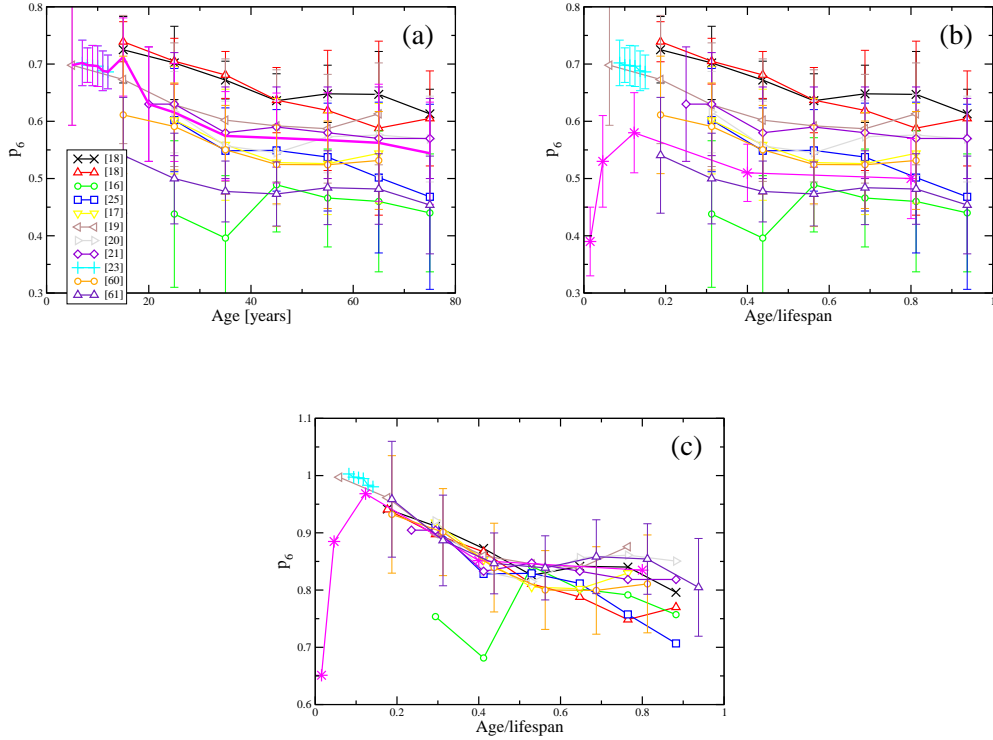


FIG. 2. Experimental data showing the change in the fraction of hexagons, p_6 , with patient age. In panel (a) the data are shown for human subjects. The thick magenta line shows the mean average behaviour. In panel (b) the human patient data are shown as a function of a reduced time obtained by division by a typical life expectancy (here $t_{exp} \simeq 80$ years). For comparison the figure also shows data for mice (from ref.²²) divided by their life expectancy of $t_{exp} \simeq 2.5$ years. In panel (c) the data from (b) are shown (again as a function of reduced age) but normalised such that $p_6 \rightarrow 1$ as $t \rightarrow 0$. In all cases the respective references are shown in the legend.

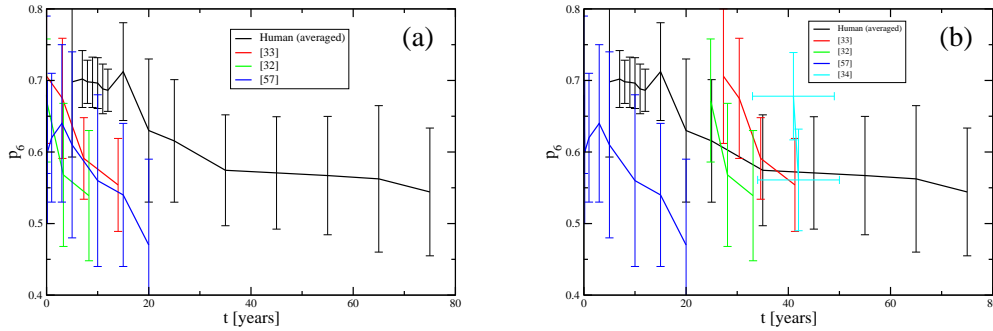


FIG. 3. Experimental data for the time dependence of the fraction of hexagons, p_6 . The solid black line shows the mean average behaviour from human patients (as shown in figure 2). The red and green lines show the effect of contact lens wearing over time whilst the blue line shows the analogous change in transplanted corneas. In panel (a) time corresponds to the patient age for the black line but the time since starting wearing contact lenses or since the transplant for the three other lines. In panel (b) the data for contact lens wearing has been offset along the abscissa by the mean age of the patients on beginning contact lens use. In both cases the respective references are shown in the legend.

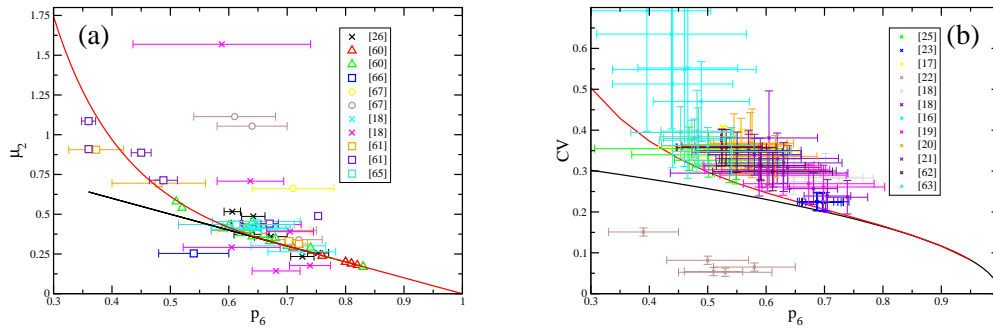


FIG. 4. Experimental data for, (a), the variance, μ_2 , and, (b), the coefficient of variation of the area, $CV (= \sigma_A/\bar{A})$, for which more complete ring size distribution data is available. In both panels the ideal (maximum entropy) solutions for the constrained 5-, 6- and 7-membered ring system and unconstrained ring size system are shown as black and red solid lines respectively. In both cases the respective references are shown in the legend.

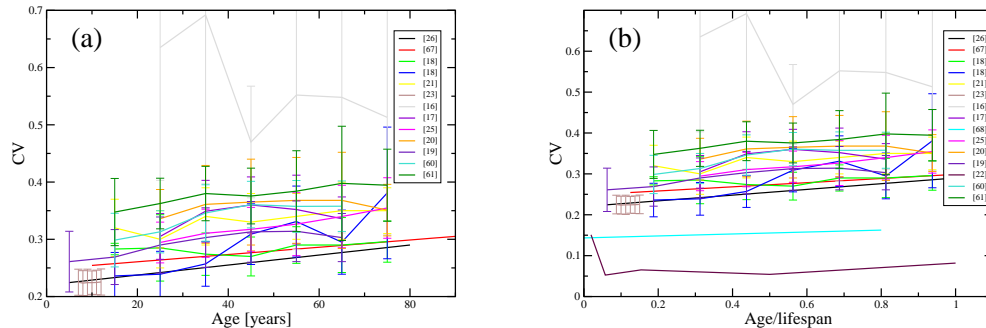


FIG. 5. Experimental data showing the change in the coefficient of variation of the area, CV , as a function of human patient age. In panel (a) the abscissa is shown in years whilst in panel (b) the abscissa is shown divided by lifespan (as in figure 2) and additional data for mice²² and cats⁶⁸ are shown. In both cases the respective references are shown in the legend.

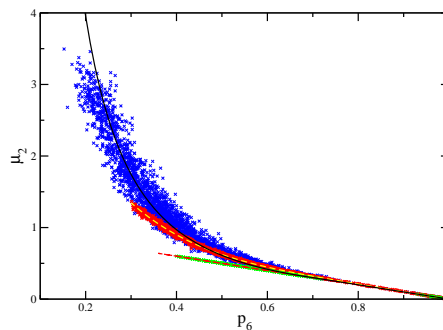


FIG. 6. Lemaitre curve plot of the variance, μ_2 , against fraction of hexagons, p_6 , obtained from the models at three levels of constraint. The green, red, and blue points show data collected from models constrained to have 5-, 6- and 7-membered rings only, 4- to 8-membered rings (inclusive) only, and unconstrained ring size distributions respectively. The ideal (maximum entropy) solutions for the constrained 5-, 6- and 7-membered ($\{567\}$) ring system, constrained $\{45678\}$ ring system, and unconstrained ring size system are shown as dashed red, dashed yellow and solid lines respectively.

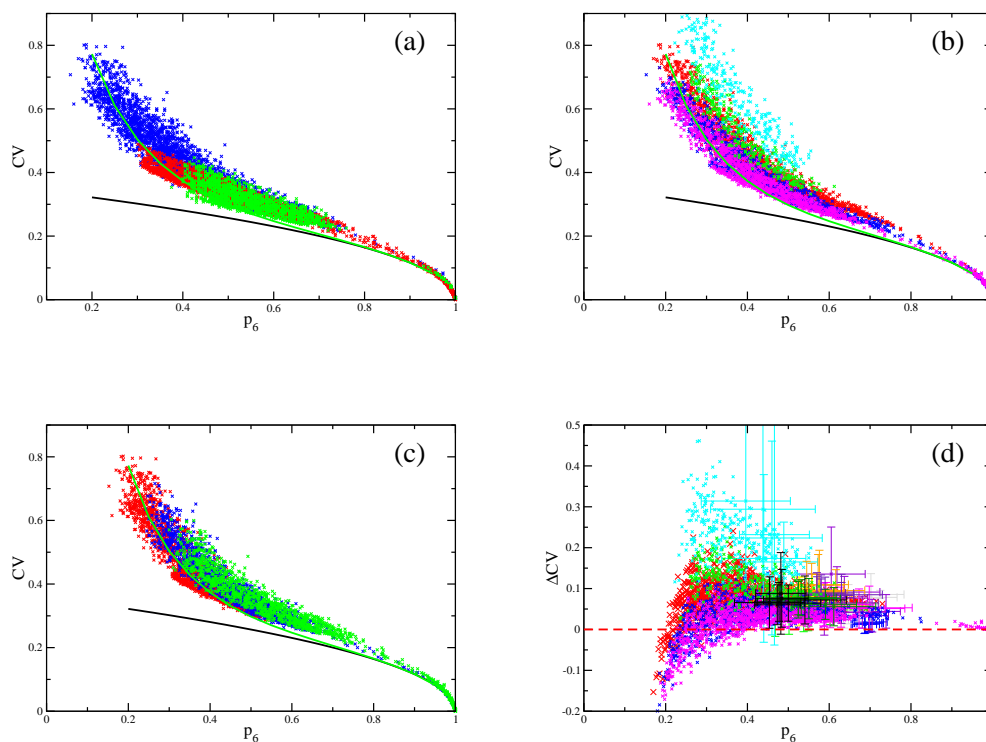


FIG. 7. The coefficients of variation for the polygon area obtained from the simulation models. Panel (a) shows the values obtained from the models at three levels of constraint. The green, red, and blue points show data collected from models constrained to have 5-, 6- and 7-membered rings only ($\{567\}$), 4- to 8-membered rings (inclusive) only ($\{45678\}$), and unconstrained ring size distributions respectively. Panels (b) and (c) show the CV values for fixed values of k_r and k_θ respectively. Panel (b) key: $k_r = 0.01, 0.1, 0.2, 0.6, 1.0$ - cyan, green, red, blue and magenta crosses respectively. Panel (c) key: $k_\theta = 0.1, 0.2, 0.3$ - red, blue and green crosses respectively. In panels (a)-(c) the solid black and green lines correspond to ideal values for the $\{567\}$ constrained and unconstrained systems respectively. Panel (d) shows the excess CV, ΔCV , at fixed k_r (key as for panel (b)). Panel (d) also shows the values for ΔCV obtained from the experimental data highlighted in figure 4(b) with the same key.

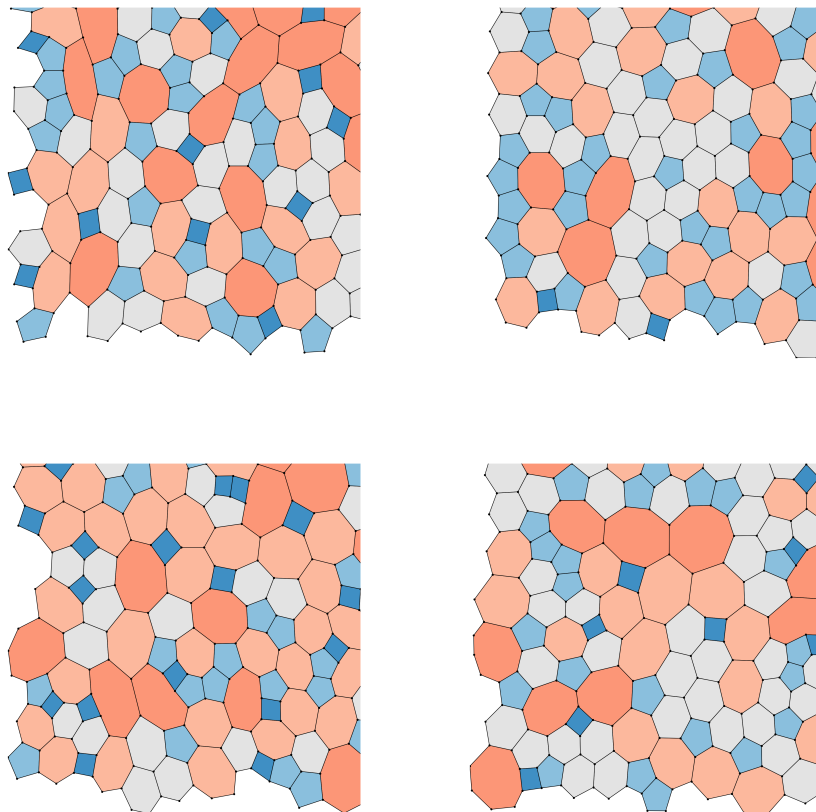


FIG. 8. Molecular graphics “snapshots” showing four configurations which vary by the ratio of the angular and bond force constants, k_θ/k_r . Different ring sizes are shown in different colours. Key (k_θ/k_r): top left - 0.1, top right - 0.3, bottom left - 0.5, bottom right - 1.5.

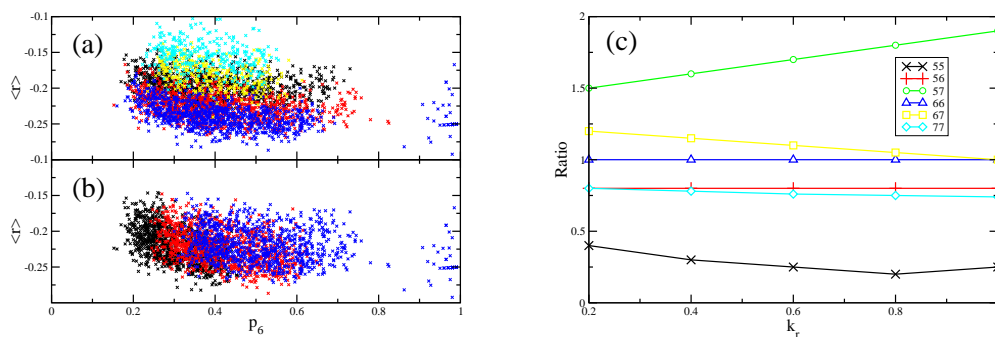


FIG. 9. The left panels show the assortativities, r , at (a) fixed k_r whilst varying k_θ , and (b) fixed k_θ whilst varying k_r . Key: (a) $k_r = 0.01$ (cyan), 0.1 (yellow), 0.2 (black), 0.6 (red), 1.0 (blue). (b) $k_\theta = 0.1$ (black), 0.2 (red), 0.3 (blue). The right panel (c) shows the nearest-neighbour ring adjacencies for $k_\theta = 0.2$ as a function of k_r displayed as the ratio of the observed number of nearest-neighbour pairs for rings sizes k and k' and the expected number assuming a random distribution of rings. The legend indicates the values of the rings sizes, k and k' .

- ¹ C. Oyster, *The Human Eye: Structure and Function* (Sinauer Associates Inc., 1999).
- ² D. DelMonte and T. Kim, *J. Cataract Refract. Surg.* **37**, 588 (2011).
- ³ P. Y. Huang, S. Kurasch, A. Srivastava, V. Skakalova, J. Kotakoski, A. V. Krashennnikov, R. Hovden, Q. Mao, J. C. Meyer, J. H. Smet, *et al.*, *Nano Lett.* **12**, 1081 (2012).
- ⁴ C. Büchner and M. Heyde, *Prog. Surf. Sci.* **92**, 341 (2017).
- ⁵ A. W. Robertson, G.-D. Lee, K. He, E. Yoon, A. I. Kirkland, and J. H. Warner, *Nano Lett.* **14**, 3972 (2014).
- ⁶ J. C. Earnshaw and D. J. Robinson, *Phys. Rev. Lett.* **72**(23), 3682 (1994).
- ⁷ C. Allain and L. Limat, *Phys. Rev. Lett.* **74**(15), 2981 (1995).
- ⁸ M. Durand, J. Käfer, C. Quilliet, S. Cox, S. A. Talebi, and F. Graner, *Phys. Rev. Lett.* **107**, 168304 (2011).
- ⁹ M. Tong, K. Cole, P. R. Brito-Parada, S. Neethling, and J. J. Cilliers, *Langmuir* **33**, 3839 (2017).
- ¹⁰ M. C. Gibson, A. B. Patel, R. Nagpal, and N. Perrimon, *Nature* **442**, 1038 (2006).
- ¹¹ R. Carter, Y. E. Sánchez-Corrales, M. Hartley, V. A. Grieneisen, and A. F. M. Marée, *Development* **144**, 4386 (2017).
- ¹² L. Goehring and S. W. Morris, *Phys. Today* **67**(11), 39 (2014).
- ¹³ A.-I. Barabási, *Nat. Phys.* **8**, 14 (2012).
- ¹⁴ S. Boccaletti, V. Latora, Y. Moreno, M. Chavez, and D.-U. Hwang, *Phys. Rep.* **424**, 175 (2006).
- ¹⁵ S. H. Strogatz, *Nature* **410**, 268 (2001).
- ¹⁶ P. Mohd Salih, *Med. J. Malaysia* **66**, 300 (2011).
- ¹⁷ C. Arici, O. Arslan, and F. Dikkaya, *J. Opht.* **2014**, 852624 (2014).
- ¹⁸ M. Matsuda, R. Yee, and H. Edelhauser, *Arch. Ophthalmol.* **103**, 68 (1985).
- ¹⁹ T. Ono, Y. Mori, R. Nejima, T. Iwasaki, T. Miyal, and K. Miyata, *Sci. Rep.* **11**, 18224 (2021).
- ²⁰ S. Rao, P. Sen, R. Fogla, S. Gangadharan, P. Padmanabhan, and S. Badrinath, *Cornea* **19**, 820 (2000).
- ²¹ H. Yunliang, S. amd Yuqiang, L. Ying-peng, Z. Ming-zhi, D. Lam, and S. Rao, *Clinical Science* **26**, 130 (2007).
- ²² S. Jun, A.S. amd Chakravarti, H. Edelhauser, and M. Kimos, *Exp. Eye Res.* **83**, 890 (2006).
- ²³ H. Al Farhan, W. Albaow, and W. Masoud, *J. Egypt Opht. Soc.* **107**, 63 (2014).
- ²⁴ A. Müller, M. Doughty, and L. Wright, *Br. J. Ophthalmol.* **82**, 692 (2000).
- ²⁵ M. Abdellah, H. Ammar, M. Anbar, E. Mostafa, M. Farouk, K. Sayed, A. Alsmman, and M. Elghobaier, *J. Opht.* **2019**, 6370241 (2019).
- ²⁶ R. Yee, M. Matsuda, R. Schultz, and H. Edelhauser, *Curr. Eye Res.* **4**, 671 (1985).
- ²⁷ B. Chowdhury, S. Bhadra, P. Mittal, and K. Shyam, *Indian J. Opht.* **69**, 1718 (2021).
- ²⁸ Y. Kim and T. Kim, *Sci. Rep.* **11**, 8324 (2021).
- ²⁹ J. Lee, B. Oum, H. Choi, J. Lee, and B. Cho, *Eye* **20**, 315 (2006).
- ³⁰ N. Tasli, Y. Icel, E. amd Karakurt, T. Ucak, A. Ugurlu, H. Yilmaz, and E. Akbaqs, *BMC Opht.* **20**, 214 (2020).
- ³¹ K. Golabchi, M.-A. Abtahi, A. Salehi, H. Jahanbani-Ardakani, S. Ghaffari, and Z. Farajzadegan, *Cut. Ocu. Toxi.* **37**, 9 (2017).
- ³² S.-W. Chang, F.-W. Hu, and L.-K. Lin, *Ophthalmologica* **215**, 197 (2001).
- ³³ J. Lee, S. Park, W.S. amd Lee, B. Oum, and B. Cho, *Gra. Arch. Clin. Exp. Opht.* **239**, 1 (2001).
- ³⁴ C. Nieuwendaal, M. Odenthal, J. Kok, H. Venema, J. Oosting, F. Riemsdag, and A. Kijlstra, *Invest Ophthalmol. Vis. Sci.* **35**, 3071 (1994).
- ³⁵ M. Odenthal, I. Gan, J. Oosting, A. Kijlstra, and W. Beekhuis, *Clinical Science* **24**, 32 (2005).
- ³⁶ M. E. Newman, *Phys. Rev. Lett.* **89**(20), 1 (2002).
- ³⁷ R. Noldus and P. V. Mieghem, *J. Complex Networks* **3**, 507 (2015).
- ³⁸ A. Chremos and P. J. Camp, *Phys. Rev. E* **76**, 056108 (2007).
- ³⁹ A. Gervois, J. P. Troadec, and J. Lemaitre, *J. Phys. A* **25**, 6169 (1992).
- ⁴⁰ D. Ormrod Morley, A. Thornework, R. Dullens, and M. Wilson, *Phys. Rev. E* **101**, 042309 (2020).
- ⁴¹ A. Malashevich, S. Ismail-Beigi, and E. I. Altman, *J. Phys. Chem. C* **120**, 26770 (2016).
- ⁴² D. Ormrod Morley, A. L. Goodwin, and M. Wilson, *Phys. Rev. E* **102**(6), 062308 (2020).
- ⁴³ D. A. Aboav, *Metallography* **3**, 383 (1970).
- ⁴⁴ D. Weaire, *Metallography* **7**, 157 (1974).
- ⁴⁵ J. K. Mason, R. Ehrenborg, and E. A. Lazar, *J. Phys. A* **45**, 065001 (2012).
- ⁴⁶ F. Wooten, K. Winer, and D. Weaire, *Phys. Rev. Lett.* **54**(13), 1392 (1985).
- ⁴⁷ V. Meunier, A. G. Souza Filho, E. B. Barros, and M. S. Dresselhaus, *Rev. Mod. Phys.* **88**, 025005 (2016).
- ⁴⁸ J. M. Greneche and J. M. D. Coey, *J. Phys. Fr.* **51**(3), 231 (1990).
- ⁴⁹ N. Metropolis, A. W. Rosenbluth, M. N. Rosenbluth, A. H. Teller, and E. Teller, *J. Chem. Phys.* **21**(6), 1087 (1953).
- ⁵⁰ D. Weaire and N. Rivier, *Contemp. Phys.* **50**(1), 199 (2009).
- ⁵¹ A. J. Stone and D. J. Wales, *Chem. Phys. Lett.* **128**(5), 501 (1986).
- ⁵² S. von Althan, A. Kuronen, and K. Kaski, *Phys. Rev. B* **68**, 073203 (2003).
- ⁵³ M. Bulacu, N. Goga, W. Zhao, G. Rossi, L. Monticelli, X. Periole, D. P. Tieleman, and S. J. Marrink, *J. Chem. Theory Comput.* **9**, 3282 (2013).
- ⁵⁴ F. Wooten and D. Weaire, *J. Non-Cryst. Solids* **64**, 325 (1984).
- ⁵⁵ R. M. Martin, *Phys. Rev. B* **1**, 4005 (1970).
- ⁵⁶ A. Kumar, M. Wilson, and M. F. Thorpe, *J. Phys. Condens. Matter* **24**, 485003 (2012).

- ⁵⁷ W. Bourne, *Cornea* **20**, 560 (2001).
- ⁵⁸ W. Bourne, D. Hodge, and L. Nelson, *Am. J. Ophthalmol.* **118**, 185 (1994).
- ⁵⁹ M. Matsuda, R. Yee, D. Glasser, D. Geroski, and H. Edelhauser, *Arch. Ophthalmol.* **104**, 259 (1986).
- ⁶⁰ R. Yee, M. Matsuda, T. Kern, R. Engerman, and H. Edelhauser, *Curr. Eye Res.* **4**, 759 (1985).
- ⁶¹ R. Yee, D. Geroski, E. Champeau, L. Meyer, and H. Edelhauser, *Invest Ophthalmol. Vis. Sci.* **26**, 1191 (1985).
- ⁶² Q. Ul Islam, M. K. Saeed, and M. Mehboob, *Saudi J. Opht.* **31**, 86 (2017).
- ⁶³ N. Tananuvat and N. Khumchoo, *BMC Opht.* **20**, 167 (2020).
- ⁶⁴ K. Carlson, W. Bourne, and R. Brubaker, *Invest Ophthalmol. Vis. Sci.* **29**, 185 (1988).
- ⁶⁵ M. Doughty, *Ophtal. Physiol. Opt.* **18**, 415 (1998).
- ⁶⁶ J. González-Méijome, J. Jorge, A. Queirós, S. Peixoto-de Matos, and M. Parafita, *Graefes Arch. Clin. Exp. Ophthalmol.* **248**, 1159 (2010).
- ⁶⁷ K. Carlson, W. Bourne, J. McLaren, and R. Brubaker, *Exp. Eye Res.* **47**, 27 (1988).
- ⁶⁸ T. Chan-ling and J. Curmi, *Curr. Eye Res.* **7**, 387 (1988).
- ⁶⁹ The data for p_6 and CV given in table I of ref.¹⁶ may have been swapped in the original publication.
- ⁷⁰ Assuming $r_0 = 1$ then $A_5 \sim 1.67$ and $A_7 \sim 3.53$.

(a)

